Very high order P_NP_M schemes on unstructured meshes for the resistive relativistic MHD equations

Michael Dumbser [a,*], Olindo Zanotti [b]

[a] *Laboratory of Applied Mathematics, University of Trento, Via Mesiano 77, I-38100 Trento, Italy*
[b] *Max-Planck-Institut für Gravitationsphysik, Albert Einstein Institut, Am Mühlenberg 1, D-14476 Golm, Germany*

ARTICLE INFO

ABSTRACT

In this paper we propose the first better than second order accurate method in space and time for the numerical solution of the resistive relativistic magnetohydrodynamics (RRMHD) equations on unstructured meshes in multiple space dimensions. The nonlinear system under consideration is purely hyperbolic and contains a source term, the one for the evolution of the electric field, that becomes stiff for low values of the resistivity.

For the spatial discretization we propose to use high order P_NP_M schemes as introduced in Dumbser et al. [M. Dumbser, D. Balsara, E.F. Toro, C.D. Munz, A unified framework for the construction of one-step finite volume and discontinuous Galerkin schemes, Journal of Computational Physics 227 (2008) 8209–8253] for hyperbolic conservation laws and a high order accurate unsplit time-discretization is achieved using the element-local space–time discontinuous Galerkin approach proposed in Dumbser et al. [M. Dumbser, C. Enaux, E.F. Toro, Finite volume schemes of very high order of accuracy for stiff hyperbolic balance laws, Journal of Computational Physics 227 (2008) 3971–4001] for one-dimensional balance laws with stiff source terms. The divergence-free character of the magnetic field is accounted for through the divergence cleaning procedure of Dedner et al. [A. Dedner, F. Kemm, D. Kröner, C.-D. Munz, T. Schnitzer, M. Wesenberg, Hyperbolic divergence cleaning for the MHD equations, Journal of Computational Physics 175 (2002) 645–673].

To validate our high order method we first solve some numerical test cases for which exact analytical reference solutions are known and we also show numerical convergence studies in the stiff limit of the RRMHD equations using P_NP_M schemes from third to fifth order of accuracy in space and time. We also present some applications with shock waves such as a classical shock tube problem with different values for the conductivity as well as a relativistic MHD rotor problem and the relativistic equivalent of the Orszag–Tang vortex problem. We have verified that the proposed method can handle equally well the resistive regime and the stiff limit of ideal relativistic MHD. For these reasons it provides a powerful tool for relativistic astrophysical simulations involving the appearance of magnetic reconnection.

1. Introduction

Although the assumption of infinite conductivity is often justified in astrophysics, there are nevertheless situations in which neglecting the resistivity of the plasma may lead to rather inaccurate or simply wrong conclusions. This is particularly the case for those physical systems involving processes that present magnetic reconnection, such as in the magnetospheres

of pulsars near the Y-point, where the outermost magnetic field lines intersect the equatorial plane [16,34]; or in soft gamma-ray repeaters where giant flares could be the explanation of the observed strongly magnetized and relativistic ejection events [26]; or in extragalactic jets, where particle acceleration by magnetic reconnection in electron–positron plasmas is supposed to take place [18,31], and also in active galactic nuclei, where Petschek magnetic reconnection, associated with MHD turbulence, may generate violent releases of energy [9]. Moreover, the presence of relativistic motion makes resistive effects quantitatively and qualitatively different from those encountered in the Newtonian regime. For example, the relativistic reconnection of Petschek type with non-strictly parallel reconnecting fields produces a strong compression of the plasma and the energy of the reconnecting field can be largely propagated away in the form of a Poynting flux [25]. In addition, the reconnection rate is also affected, and it is roughly obtained by replacing the Alfvén wave velocity with the speed of light in the corresponding formulas.

For all these reasons, and moreover because the question on whether relativistic magnetic reconnection is an efficient energy converter is still under debate (see the discussion in [27,37]) there is a strong interest in the numerical solution of the full system of RRMHD, by providing a single computational tool that can equally well handle situations of low and high resistivity, as commonly encountered in all realistic physical scenarios. The equations to solve are particularly challenging from the numerical point of view, since, as recently shown by [23,29], they become stiff for large values of the conductivity. Namely, the RRMHD equations can be cast into the following general form of a hyperbolic balance law

$$\frac{\partial}{\partial t} W + \nabla \cdot \mathbf{F}(W) = S(W), \tag{1}$$

where W is the state vector, $\mathbf{F}(W)$ is a nonlinear flux tensor that depends on the state W and $S(W)$ is a nonlinear source term that becomes stiff at high conductivities. In this paper we solve the RRMHD equations by applying the high order accurate method recently proposed by Dumbser et al. [11] to cope with stiff source terms on the right-hand side of (1) and maintaining at the same time better than second order of accuracy in space and time. The numerical method is formulated as one-step local predictor global corrector method. The predictor is based on an element-local weak solution of (1), where inside each element the governing PDE (1) is solved *in the small* (see [17]) by means of a locally implicit space–time discontinuous Galerkin scheme. This leads to an algebraic system of non-linear equations that must be solved individually for each element. The globally explicit update in time, on the other hand, is obtained by either standard finite volume or discontinuous Galerkin methods, or, finally, by a recently proposed generalization of the two named $P_N P_M$ schemes according to [10].

The plan of the paper is as follows. In Section 2 we briefly review the peculiar features of the RRMHD equations. The core of the numerical method is described in Section 3 while Section 4 is devoted to the validation of the scheme through a large class of numerical tests. Finally, the conclusions are reported in Section 5. We have considered only flat space–times in pseudo-Cartesian coordinates, namely the metric $\eta_{\mu\nu} = \mathrm{diag}(-1, 1, 1, 1)$, where from now onwards we agree to use Greek letters $\mu, \nu, \lambda, \ldots$ (running from 0 to 3) for indices of four-dimensional space–time tensors, while using Latin letters $i, j, k, \ldots$ (running from 1 to 3) for indices of three-dimensional spatial tensors. Finally, we set the speed of light $c = 1$ and make use of the Lorentz–Heaviside notation for the electromagnetic quantities, such that all $\sqrt{4\pi}$ factors disappear. We use Einstein summation convention over repeated indices.

2. The resistive relativistic MHD equations

2.1. Conservative formulation as a stiff hyperbolic balance law

The total energy-momentum tensor of the system is made up by two contributions, $T^{\mu\nu} = T_m^{\mu\nu} + T_f^{\mu\nu}$. The first one is due to matter

$$T_m^{\mu\nu} = \omega u^\mu u^\nu + p\eta^{\mu\nu}, \tag{2}$$

where u^μ is the four velocity of the fluid, while ω and p are the enthalpy and the pressure as measured in the co-moving frame of the fluid. The second contribution is due to the electromagnetic field

$$T_f^{\mu\nu} = F_\lambda^\mu F^{\nu\lambda} - \frac{1}{4}(F^{\lambda\kappa} F_{\lambda\kappa})\eta^{\mu\nu}, \tag{3}$$

where $F^{\mu\nu}$ is the electromagnetic tensor given by

$$F^{\mu\nu} = n^\mu E^\nu - E^\mu n^\nu + \epsilon^{\mu\nu\lambda\kappa} B_\lambda n_\kappa. \tag{4}$$

E^ν and B^ν are the electric and magnetic field as measured by the observer defined by the four-velocity vector n^μ, while $\epsilon^{\mu\nu\lambda\kappa} = [\mu\nu\lambda\kappa]$ is the completely antisymmetric space–time Levi–Civita tensor, with the convention that $\epsilon^{0123} = 1$. If we now set n^μ to define the inertial laboratory observer, namely $n^\mu = (1, 0, 0, 0)$, normalized such that $n^\mu n_\mu = -1$, then the four vectors of the electric and of the magnetic field are purely spatial, i.e. $E^0 = B^0 = 0$, $E^i = E_i$, $B^i = B_i$. On the other hand, the fluid four velocity u^μ and the standard three velocity in the laboratory frame are related as $\vec{v} = v^i = u^i/\Gamma$, where $\Gamma = (1 - \vec{v}^2)^{-0.5}$ is the Lorentz factor of the fluid with respect to the laboratory frame. The equations of motion can be derived from the conservation laws

$$\partial_\mu T^{\mu\nu} = 0 \tag{5}$$

and from the continuity equation

$$\partial_\mu(\rho u^\mu) = 0, \tag{6}$$

where ρ is the rest mass density of the fluid. The electromagnetic field, on the other hand, obeys the Maxwell equations expressed in the form

$$\partial_\mu F^{*\mu\nu} = 0, \quad \partial_\nu F^{\mu\nu} = I^\mu, \tag{7}$$

where $F^{*\mu\nu} = \frac{1}{2}\epsilon^{\mu\nu\lambda\kappa}F_{\lambda\kappa}$ is the dual of the electromagnetic tensor, while I^μ is the four vector of electric currents. The equations of resistive MHD differ from those of ideal MHD mainly because the second couple of Maxwell equations (7), accounting for the time evolution and for the divergence of the electric field, need to be explicitly solved. This requires that a relation is given between the currents and the electromagnetic field, the so-called Ohm's law. In its most general form, the relativistic formulation of Ohm's law is a non-linear propagation equation [20], but here, as in [23], we will simply assume that

$$I^\mu = q_0 u^\mu + \sigma F^{\mu\nu}u_\nu, \tag{8}$$

where q_0 is the charge density in the co-moving frame while σ is the electric conductivity. From (8) we easily derive the following expression for the spatial current vector:

$$\vec{J} = \rho_c\vec{v} + \sigma\Gamma[\vec{E} + \vec{v}\times\vec{B} - (\vec{E}\cdot\vec{v})\vec{v}], \tag{9}$$

where ρ_c is the charge density in the laboratory frame. As done by [23,29], to whom we address the reader for further details, we take care of the divergence-free character of the magnetic field by adopting the *divergence cleaning approach* presented in [7], namely by introducing two additional scalar fields Ψ and Φ that propagate away the deviations of the divergences of the electric and of the magnetic fields from the values prescribed by Maxwell's equations. In total, the full set of RRMHD equations include the five equations for the fluid, plus the six equations for the evolution of the electric and of the magnetic field, plus the two equations about the divergences of the two fields, plus one more equation expressing the conservation of the total charge. In Cartesian coordinates, using the abbreviations $\partial_t = \frac{\partial}{\partial t}$ and $\partial_i = \frac{\partial}{\partial x_i}$, they can be written as:

$$\partial_t D + \partial_i(Dv^i) = 0, \tag{10}$$

$$\partial_t S_j + \partial_i Z_j^i = 0, \tag{11}$$

$$\partial_t \tau + \partial_i S^i = 0, \tag{12}$$

$$\partial_t E^i - \epsilon^{ijk}\partial_j B_k + \partial_i\Psi = -J^i, \tag{13}$$

$$\partial_t B^i + \epsilon^{ijk}\partial_j E_k + \partial_i\Phi = 0, \tag{14}$$

$$\partial_t\Psi + \partial_i E^i = \rho_c - \kappa\Psi, \tag{15}$$

$$\partial_t\Phi + \partial_i B^i = -\kappa\Phi, \tag{16}$$

$$\partial_t\rho_c + \partial_i J^i = 0, \tag{17}$$

where the conservative variables of the fluid are

$$D = \rho\Gamma, \tag{18}$$

$$S^i = \omega\Gamma^2 v^i + \epsilon^{ijk}E_j B_k, \tag{19}$$

$$\tau = \omega\Gamma^2 - p + \frac{1}{2}(E^2 + B^2), \tag{20}$$

expressing, respectively, the relativistic mass density, the momentum density and the total energy density. The spatial tensor Z_j^i in (11), representing the momentum flux density, is

$$Z_j^i = \omega\Gamma^2 v^i v_j - E^i E_j - B^i B_j + \left[p + \frac{1}{2}(E^2 + B^2)\right]\delta_j^i, \tag{21}$$

where δ_j^i is the Kronecker delta. In the rest of the paper we have assumed the equation of state of an ideal gas, namely

$$p = (\gamma - 1)\rho\epsilon = \gamma_1(\omega - \rho), \tag{22}$$

where γ is the adiabatic index, $\gamma_1 = (\gamma - 1)/\gamma$, ϵ is the specific internal energy and $\omega = \rho\epsilon + \rho + p$ is the enthalpy. The system of Eqs. (10)–(17) is written as a hyperbolic system of balance laws as in (1), it has source terms in the three Eq. (13) that are potentially stiff (see [29] for a more detailed description of the different limits of the resistive MHD equations) and, as such, it can be treated with the procedure proposed by Dumbser et al. [11], as we will show in Section 3.

2.2. Closed form recovering of the primitive variables from the conservative ones

A fundamental difference with respect to the ideal MHD case is that the augmented set of conservative variables of the resistive relativistic equations allows for the recovering of the primitive variables from the conservative ones in closed form, at least when the equation of state is that of an ideal gas. This can be seen in the following way. Firstly, we shift the cross product $\vec{E} \times \vec{B}$ from the right-hand side to the left-hand side of Eq. (19), then we square it, and we obtain

$$(\vec{S} - \vec{E} \times \vec{B})^2 = \omega^2 \Gamma^2 (\Gamma^2 - 1). \tag{23}$$

On the other hand, from (20) we obtain the enthalpy ω as

$$\omega = \frac{\tau - \frac{1}{2}(E^2 + B^2) - \gamma_1 D/\Gamma}{\Gamma^2 - \gamma_1}, \tag{24}$$

where we have used $p = \gamma_1(\omega - \rho)$ as in (22). After replacing (24) into (23), simple calculations lead to the following quartic equation in the unknown Lorentz factor Γ as follows:

$$A_4 \Gamma^4 + A_3 \Gamma^3 + A_2 \Gamma^2 + A_1 \Gamma + A_0 = 0, \tag{25}$$

where

$$A_4 = C_1 - C_2^2, \quad A_3 = 2C_2 \gamma_1 D, \quad A_2 = C_2^2 - 2C_1 \gamma_1 - \gamma_1^2 D^2, \tag{26}$$

$$A_1 = -2C_2 \gamma_1 D, \quad A_0 = \gamma_1^2 (C_1 + D^2), \tag{27}$$

with $C_1 \equiv (\vec{S} - \vec{E} \times \vec{B})^2$, and $C_2 \equiv \tau - \frac{1}{2}(E^2 + B^2)$. The quartic (25) can be solved either analytically using the approach of Ferrari and Cardano [5] or numerically via a Newton–Raphson scheme. In our numerical experiments we found that for the purpose of accuracy and robustness, it is advisable to solve the quartic first analytically and then to improve the accuracy of the result by one or two additional Newton iterations. This is necessary since the computations of the roots for the analytical solution of the quartic may introduce a significant amount of roundoff errors on finite precision computer hardware even when using double precision arithmetic. It is only for this reason that the additional Newton iterations are performed. This step would not be necessary with exact arithmetic.

As already pointed out by Zenitani et al. [37], it turns out that (25) has two complex conjugate solutions, plus two real solutions, of which only one is larger than unity, as physically required. Once the Lorentz factor is known, the other primitive variables can be computed in a straightforward manner.

3. Numerical method

3.1. The $P_N P_M$ reconstruction operator on unstructured meshes

The main ingredient of the proposed numerical method to reach high order of accuracy in space is the $P_N P_M$ reconstruction operator on unstructured meshes first introduced in [10]. It is a direct extension of the reconstruction algorithm proposed in [12,13] for finite volume schemes. For the details, we refer to the above mentioned publications and give only a short review in this section. The computational domain Ω is discretized by conforming elements Q_i, indexed by a single mono-index i ranging from 1 to the total number of elements N_E. The elements are chosen to be triangles in 2D and tetrahedrons in 3D. The union of all elements is called the triangulation or tetrahedrization of the domain, respectively,

$$\mathcal{Q}_\Omega = \bigcup_{i=1}^{N_E} Q_i. \tag{28}$$

At the beginning of a time-step, the numerical solution of (1) for the state vector W, denoted by u_h, is represented by piecewise polynomials of degree N from the space V_h, spanned by the basis functions $\Phi_l = \Phi_l(\vec{x})$, i.e. at $t = t^n$ we have for each element

$$u_h(\vec{x}, t^n) = \sum_l \Phi_l(\vec{x}) \hat{u}_l^n. \tag{29}$$

From the polynomials u_h, we then reconstruct piecewise polynomials w_h of degree $M \geqslant N$ from the space W_h, spanned by the basis functions $\Psi_l = \Psi_l(\vec{x})$:

$$w_h(\vec{x}, t^n) = \sum_l \Psi_l(\vec{x})\hat{w}_l^n. \tag{30}$$

As stated in [10], the Ψ_l form an orthogonal basis and are identical with the Φ_l up to polynomial degree N. For performing the reconstruction on element Q_i, we now choose a reconstruction stencil

$$\mathcal{S}_i = \bigcup_{k=1}^{n_e} Q_{j(k)} \tag{31}$$

that contains a total number of n_e elements. Here $1 \leqslant k \leqslant n_e$ is a local index, counting the elements in the stencil, and $j = j(k)$ is the mapping from the local index k to the global indexation of the elements in $\mathcal{Q}_\Omega$. For ease of notation, we write in the following only j, meaning $j = j(k)$.

In the present paper the three operators

$$\langle f, g \rangle_{Q_i} = \int_{t^n}^{t^{n+1}} \int_{Q_i} (f(\vec{x}, t) \cdot g(\vec{x}, t))dV \, dt, \tag{32}$$

$$[f, g]_{Q_i}^t = \int_{Q_i} (f(\vec{x}, t) \cdot g(\vec{x}, t))dV, \tag{33}$$

$$\{f, g\}_{\partial Q_i} = \int_{t^n}^{t^{n+1}} \int_{\partial Q_i} (f(\vec{x}, t) \cdot g(\vec{x}, t))dS \, dt, \tag{34}$$

denote the scalar products of two functions f and g over the space–time element $Q_i \times [t^n; t^{n+1}]$, over the spatial element Q_i, and over the space–time boundary element $\partial Q_i \times [t^n; t^{n+1}]$, respectively. The operators $\langle f, g \rangle$ and $[f, g]^t$, written without the index Q_i, will denote scalar products on the space–time reference element $Q_E \times [0; 1]$ and on the spatial reference element Q_E at time t, respectively. The spatial reference element Q_E is defined as the unit simplex with vertices $(0,0)$, $(1,0)$, $(0,1)$ in two space dimensions and vertices $(0,0,0)$, $(1,0,0)$, $(0,1,0)$ and $(0,0,1)$ in three space dimensions, respectively.

The reconstruction is now obtained via L_2-projection of the (unknown) piecewise polynomials w_h from the space W_h into the space V_h on each stencil $\mathcal{S}_i$ as follows:

$$[\Phi_k, w_h]_{Q_j}^{t^n} = [\Phi_k, u_h]_{Q_j}^{t^n}, \quad \forall Q_j \in \mathcal{S}_i. \tag{35}$$

Note that during the reconstruction step, the polynomials w_h are continuously extended over the whole stencil $\mathcal{S}_i$. After reconstruction, the piecewise polynomials w_h are again restricted onto each element Q_i. The number of elements in the stencils are chosen in such a way that the number of equations in (35) is *larger* that the number of degrees of freedom in the space W_h. Eq. (35) constitutes thus an overdetermined linear algebraic equation system for the coefficients of w_h and is solved using a constrained least squares technique, see [10,12]. The linear constraint is that (35) is at least exactly satisfied for $Q_j = Q_i$, i.e. inside the element Q_i under consideration. The integral on the left hand side in (35) is computed using classical multidimensional Gaussian quadrature of appropriate order, see [32]. The integral on the right-hand side can be computed analytically and involves the standard element mass-matrix.

The resulting M-exact $P_N P_M$ least squares reconstruction can be interpreted as a generalization of the k-exact reconstruction proposed for pure finite volume schemes by Barth and Frederickson in their pioneering work [4].

3.2. The local space–time discontinuous Galerkin predictor for stiff balance laws

The original ENO scheme of Harten et al. [17] as well as the ADER-FV and ADER-DG schemes developed by Titarev and Toro [33] and Dumbser and Munz [14] use the governing PDE itself in its strong differential form to obtain high order of accuracy in time. This is achieved via the so-called Cauchy–Kovalewski procedure that substitutes time derivatives with space derivatives via successive differentiation of the governing PDE with respect to space and time. This procedure becomes very cumbersome or even impossible for general nonlinear hyperbolic PDE systems. In [11,10,3] an fully numerical approach was presented that replaces the semi-analytical Cauchy–Kovalewski procedure by a *local weak formulation* of the governing PDE in space–time. While the approach presented in [11] relies on a local discontinuous Galerkin approach in space–time, which is also able to handle stiff source terms, the methods proposed in [10] uses a local continuous Galerkin method in space–time as predictor. In the present article we use the local space–time discontinuous Galerkin method due to the stiffness of the source terms.

We underline that the local space–time DG method is only used as *local predictor* for the construction of a solution of the PDE *in the small*, as it was called by Harten et al. in [17]. The local space–time predictors are then inserted into a *global corrector*, which is fully explicit and provides the coupling between neighbor cells. As a consequence, the resulting nonlinear algebraic systems of the local space–time Galerkin methods are element-local and not globally coupled, as in the global and fully implicit space–time Galerkin approach introduced by van der Vegt and van der Ven [35,21].

The details of the local space–time DG predictor method are already given in [11], hence we will only briefly recall the basic ideas here. We start from the strong formulation of PDE (1) and transform the PDE into the reference coordinate system $(\vec{\xi}, \tau)$ of the space–time reference element $Q_E \times [0; 1]$ with $\vec{\xi} = (\xi, \eta)$ and ∇_ξ being the nabla operator in the $\xi - \eta$ reference system:

$$\frac{\partial}{\partial \tau} W + \nabla_\xi \cdot \mathbf{F}^*(W) = S^*. \tag{36}$$

The modified flux tensor and the modified source term are given by

$$\mathbf{F}^* := \Delta t \mathbf{F}(W) J^T, \quad S^* := \Delta t S(W), \quad J = \frac{\partial \vec{\xi}}{\partial \vec{x}}, \tag{37}$$

as revealed by simple algebraic manipulations. We now multiply (36) by a space–time test function $\theta_k = \theta_k(\xi, \eta, \tau)$ from the space of piecewise space–time polynomials of degree M and integrate over the space–time reference control volume $Q_E \times [0; 1]$ to obtain the following weak formulation:

$$\left\langle \theta_k, \frac{\partial}{\partial \tau} \mathcal{W}_h \right\rangle + \langle \theta_k, \nabla_\xi \cdot \mathbf{F}_h^*(\mathcal{W}_h) \rangle = \langle \theta_k, \mathcal{S}_h^*(\mathcal{W}_h) \rangle. \tag{38}$$

In the numerical solution of Eq. (38) we use the same ansatz for $\mathcal{W}_h$ as well as for the flux tensor and the source term, i.e.

$$\mathcal{W}_h = \mathcal{W}_h(\xi, \eta, \tau) = \sum_l \theta_l(\xi, \eta, \tau) \widehat{\mathcal{W}}_l := \theta_l \widehat{\mathcal{W}}_l, \tag{39}$$

$$\mathcal{F}_h^* = \mathcal{F}_h^*(\xi, \eta, \tau) = \sum_l \theta_l(\xi, \eta, \tau) \widehat{\mathcal{F}_l^*} := \theta_l \widehat{\mathcal{F}_l^*}, \tag{40}$$

$$\mathcal{S}_h^* = \mathcal{S}_h^*(\xi, \eta, \tau) = \sum_l \theta_l(\xi, \eta, \tau) \widehat{\mathcal{S}_l^*} := \theta_l \widehat{\mathcal{S}_l^*}. \tag{41}$$

The degrees of freedom of the flux $\widehat{\mathcal{F}_l^*}$ and the source $\widehat{\mathcal{S}_l^*}$ can be computed from the ones of the state vector $\widehat{\mathcal{W}}_l$ either via the more accurate but also more expensive L^2-projection,

$$\langle \theta_l, \theta_l \rangle \widehat{\mathcal{F}_l^*} = \langle \theta_k, \mathcal{F}^*(\mathcal{W}_h) \rangle, \quad \langle \theta_l, \theta_l \rangle \widehat{\mathcal{S}_l^*} = \langle \theta_k, \mathcal{S}^*(\mathcal{W}_h) \rangle, \tag{42}$$

or in a simple and cheap nodal fashion, if a nodal space–time basis as the one in [10] is used:

$$\widehat{\mathcal{F}_l^*} = \mathcal{F}^*(\widehat{\mathcal{W}}_l), \quad \widehat{\mathcal{S}_l^*} = \mathcal{S}^*(\widehat{\mathcal{W}}_l). \tag{43}$$

In the element-local weak formulation of Eq. (38) we apply integration by parts to the first term and thus obtain

$$[\theta_k, \mathcal{W}_h]^1 - [\theta_k, w_h]^0 - \left\langle \frac{\partial}{\partial \tau} \theta_k, \mathcal{W}_h \right\rangle + \langle \theta_k, \nabla_\xi \cdot \mathcal{F}_h^* \rangle = \langle \theta_k, \mathcal{S}_h^* \rangle, \tag{44}$$

where the initial condition at relative time $\tau = 0$ is taken into account in a *weak sense* by the term $[\theta_k, w_h]^0$. We recall that w_h is the piecewise polynomial obtained by the high order $P_N P_M$ reconstruction operator summarized in 3.1. We also note that the first two terms in (44) correspond to the choice of an upwind flux in the time direction, which is consistent with the causality principle that states that no effect can occur before its cause. Inserting the ansatz (39)–(41) into (44) we obtain

$$\left([\theta_k, \theta_l]^1 - \left\langle \frac{\partial}{\partial \tau} \theta_k, \theta_l \right\rangle \right) \widehat{\mathcal{W}}_l - [\theta_k, \Psi_l]^0 \hat{w}_l^n + \langle \theta_k, \nabla_\xi \theta_l \rangle \cdot \widehat{\mathcal{F}_l^*} = \langle \theta_k, \theta_l \rangle \widehat{\mathcal{S}_l^*}. \tag{45}$$

After defining the following universal matrices (that need to be computed only once on the reference element) $\mathbf{K_1} = [\theta_k, \theta_l]^1 - \left\langle \frac{\partial}{\partial \tau} \theta_k, \theta_l \right\rangle, \mathbf{K_\xi} = \langle \theta_k, \nabla_\xi \theta_l \rangle, \mathbf{M} = \langle \theta_k, \theta_l \rangle, \mathbf{F_0} = [\theta_k, \Psi_l]^0$ we can rewrite (45) in the more compact matrix notation:

$$\mathbf{K_1} \widehat{\mathcal{W}}_l + \mathbf{K_\xi} \cdot \widehat{\mathcal{F}_l^*} = \mathbf{F_0} \hat{w}_l^n + \mathbf{M}, \widehat{\mathcal{S}_l^*}. \tag{46}$$

Eq. (46) is an element-local nonlinear algebraic system for the unknowns $\widehat{\mathcal{W}}_l$. For its solution we use the following simple iterative scheme, similar to the one proposed in [10]:

$$\widehat{\mathcal{W}}_l^{i+1} - (\mathbf{K_1})^{-1} \mathbf{M} \widehat{\mathcal{S}}_l^{*,i+1} = (\mathbf{K_1})^{-1} \mathbf{F_0} \hat{w}_l^n - (\mathbf{K_1})^{-1} \mathbf{K_\xi} \cdot \widehat{\mathcal{F}}_l^{*,i}. \tag{47}$$

As in [10] the matrices contained in $(\mathbf{K_1})^{-1} \mathbf{K_\xi}$ have the remarkable property that **all** their eigenvalues are **zero**, which makes (47) a contractive fixed point iteration in the homogeneous case (i.e. when $S = 0$) and thus existence, uniqueness and convergence to the unique solution are guaranteed by the Banach fixed point theorem. Furthermore, in the linear case, the method is even guaranteed to converge to the exact solution in $M + 1$ steps from any initial guess. In the non-homogeneous case with stiff source terms, however, it is necessary to take the source implicitly, which is done in the present paper. We use the following simplified linearized model for the implicit treatment of the source term:

$$\widehat{\mathcal{S}}_l^{*,i+1} \approx \widehat{\mathcal{S}}_l^{*,i} + \Delta t \frac{\partial S}{\partial W}\left(\widehat{\mathcal{W}}_l^{i+1} - \widehat{\mathcal{W}}_l^i\right), \quad \frac{\partial S}{\partial W} = \frac{\partial S}{\partial V}\frac{\partial V}{\partial W}, \quad \frac{\partial V}{\partial W} = \left(\frac{\partial W}{\partial V}\right)^{-1}, \tag{48}$$

where the full Jacobian matrix $\partial S/\partial W$ of the source S with respect to the conservative variables W is computed by the chain rule, taking first the derivatives with respect to the vector of primitive variables V. The derivative of V with respect to W can be computed easily by the theorem on the derivative of the inverse function. This requires obviously that the functions S and W are differentiable with respect to V, which is the case for the resistive RMHD equations. To implify the computations, however, we evaluate $\frac{\partial S}{\partial W}$ only once per iteration at the current space–time average value of $\mathcal{W}_h$.

In our numerical experiments we also found that in the very stiff case, the choice of the initial guess $\widehat{\mathcal{W}}_l^0$ seems to be very crucial. We therefore adopt the following strategy: first, we solve (47) at the first order level, which becomes a simple Newton–Raphson scheme for the space–time cell-average $\overline{\mathcal{W}}$ as

$$\bar{f} = \overline{\mathcal{W}} - S^*(\overline{\mathcal{W}}) - \bar{u}_i^n = 0, \tag{49}$$

where the initial guess $\overline{\mathcal{W}}^0 = \bar{u}_i^n$ is used for all variables apart from the electric field. For the electric field we use $\vec{E}$ obtained from the relaxation of $\vec{E}$ and $\vec{v}$ to equilibrium assuming the stiff limit $\sigma \to \infty$ and holding all the other conservative variables in $\overline{\mathcal{W}}^0$ constant. In our experiments the Newton method applied to Eq. (49) with this initial guess typically converges to machine zero (10^{-14}) after two or three iterations and is robust even for very large values of σ, such as $\sigma = 10^{12}$. The resulting cell-average $\overline{\mathcal{W}}$ is then used as initial guess for the high order space–time solution of Eq. (47), i.e. we set $\mathcal{W}_h^0 = \overline{\mathcal{W}}$.

3.3. The fully discrete $P_N P_M$ schemes

The fully discrete one-step form of the proposed $P_N P_M$ schemes is derived as follows: we first apply the operator $\langle \Phi_k, \cdot \rangle_{Q_i}$ to PDE (1) and obtain

$$\left\langle \Phi_k, \frac{\partial}{\partial t} W \right\rangle_{Q_i} + \langle \Phi_k, \nabla \cdot \mathbf{F}(W) \rangle_{Q_i} = \langle \Phi_k, S(W) \rangle_{Q_i}. \tag{50}$$

For the first term in Eq. (50) we approximate W with u_h from the space V_h and perform integration by parts in time. Note that the Φ_k do not depend on time and therefore their time derivatives vanish. For all the other terms in Eq. (50) the vector W is approximated by the solution $\mathcal{W}_h$ of the local space–time discontinuous Galerkin predictor of section 3.2. Since $\mathcal{W}_h$ will usually exhibit jumps at the element boundaries, we introduce a numerical flux to resolve these jumps. We hence obtain the following family of fully discrete one-step $P_N P_M$ schemes for PDE (1):

$$\left[\Phi_k, u_h^{n+1}\right]_{Q_i}^{t^{n+1}} - \left[\Phi_k, u_h^n\right]_{Q_i}^{t^n} - \langle \mathbf{F}_h, \nabla \Phi_k \rangle_{Q_i \setminus \partial Q_i} + \left\{\Phi_k, \mathscr{G}_{i+\frac{1}{2}}(\mathcal{W}_h^-, \mathcal{W}_h^+) \cdot \vec{n}\right\}_{\partial Q_i} = \langle \Phi_k, S(\mathcal{W}_h) \rangle_{Q_i}, \tag{51}$$

where $\mathcal{W}_h^-$ denotes the boundary extrapolated data from within element Q_i and $\mathcal{W}_h^+$ denotes the boundary extrapolated data from the neighbor, respectively. In the test sections of this paper, we use the Rusanov flux for $\mathscr{G}_{i+\frac{1}{2}}$, which in the case of the resistive relativistic MHD equations becomes particularly simple. Due to the presence of the full Maxwell equations, whose maximum eigenvalue is the speed of light, i.e. $\lambda_{\max} = 1$, it reduces to

$$\mathscr{G}_{i+\frac{1}{2}}(\mathcal{W}_h^-, \mathcal{W}_h^+) \cdot \vec{n} = \frac{1}{2}(\mathbf{F}(\mathcal{W}_h^+) + \mathbf{F}(\mathcal{W}_h^-)) \cdot \vec{n} - \frac{1}{2}(\mathcal{W}_h^+ - \mathcal{W}_h^-). \tag{52}$$

As an alternative, we also propose the following strategy, which gives slightly better results for the hydrodynamic quantities: For the evolution of the hydrodynamics, (10)–(12), one can use the HLL flux

$$\mathscr{G}_{i+\frac{1}{2}}(\mathcal{W}_h^-, \mathcal{W}_h^+) \cdot \vec{n} = \frac{(a^+ \mathbf{F}(\mathcal{W}_h^+) + a^- \mathbf{F}(\mathcal{W}_h^-)) \cdot \vec{n} - a^+ a^- (\mathcal{W}_h^+ - \mathcal{W}_h^-)}{a^+ + a^-}, \tag{53}$$

with

$$a^+ = \max\left\{0, \lambda_f^-, \lambda_f^+\right\}, \quad a^- = \max\left\{0, -\lambda_s^-, -\lambda_s^+\right\}, \tag{54}$$

where λ_f and λ_s denote the fastest and the slowest of the ideal MHD magnetosonic speeds along the direction of the flux, and computed through the exact or approximate solution of the corresponding quartic as in [8].

For a quadrature-free implementation that requires only the solution of one Riemann problem per space–time element interface we refer the reader to [10].

4. Numerical test cases

In this section we present some of the test cases of Palenzuela et al. [29] who used a second order accurate TVD scheme with IMEX Runge–Kutta time-integration on Cartesian meshes. In the rest of the section we use schemes of order better than two in space and time on unstructured triangular meshes and the constant κ in Eqs. (15) and (16) for the divergence cleaning is set equal to unity in all tests.

4.1. Large amplitude Alfvén wave

The properties of Alfvén waves in ideal relativistic MHD have been presented originally by Komissarov [22]. Based on that, a smooth unsteady test case with an exact analytical solution can be built (see [22,8]) that was solved for the first time on unstructured triangular meshes with high order $P_N P_M$ schemes in [10]. Since the resistive MHD equations tend asymptotically to the ideal ones in the stiff limit ($\sigma \to \infty$), this is an ideal test case to assess the accuracy of our scheme in the stiff limit of the governing PDE system.

The test case consists of a periodic Alfvén wave whose initial condition at $t = 0$ is chosen to be $\rho = p = 1, \vec{B} = B_0(1, \cos(kx), \sin(kx))^T, \vec{v} = -v_A/B_0 \cdot (0, B_y, B_z)^T, \vec{E} = -\vec{v} \times \vec{B}$ and $\phi = \psi = q = 0$. We furthermore use the parameters $k = 2\pi, \gamma = \frac{4}{3}$ and $B_0 = 1$, hence the advection speed of the Alfvén wave in x-direction is $v_A = 0.38196601125$ (see [8] for a closed analytical expression for v_A). The 2D computational domain is $\Omega = [0; 1] \times [0; 0.4]$ with four periodic boundary conditions, and the final time corresponding to an entire advection period is $t = 1/v_A = 2.618033988$. The initial condition represents the exact reference solution to be compared with our numerical one. Since this test case was constructed for the *ideal* relativistic MHD equations, we have to use a rather stiff value for the conductivity ($\sigma = 10^7$) in the resistive case to reproduce the ideal equations asymptotically. For the fifth order $P_1 P_4$ scheme this has shown to be not enough to get the full order of accuracy, hence in this case we even use $\sigma = 10^8$. In all our computations a *constant* Courant number of $\text{CFL} = 0.5/(2N + 1)$ is used.

A representative unstructured triangular mesh is visible in the left panel of Fig. 1 together with a surface plot of the quantity B_z. In the right panel we compare the exact solution after one period with the numerical one obtained on a very coarse mesh of eight triangles on the x-axis using the $P_1 P_4$ scheme. For this purpose, the reconstructed fourth degree polynomials are evaluated at the final time on 100 equidistant points along the x-axis in order to make use of the high order polynomial sub-cell resolution contained in each element. We emphasize the excellent agreement with the exact solution even on this very coarse mesh. Note that with the TVD scheme used in [29] there were clearly visible errors even on a fine mesh using 50 points along the x-axis.

Table 1 shows the errors and the orders of convergence measured in the L^2 norm for the flow variable B_y. The number N_G denotes the number of triangle edges along the x-axis. We stress that the $P_1 P_4$ scheme on the very coarse mesh with $N_G = 8$ allows to achieve an accuracy higher than the $P_0 P_2$ scheme on the finest mesh with $N_G = 64$. The nominal order of accuracy $M + 1$ has been reached for all $P_N P_M$ schemes under consideration. In [29] it was reported that when using IMEX Runge–Kutta schemes for time-discretization the authors encountered problems with the convergence rates for the relaxed variables, i.e. for the electric field that suffers from the presence of the stiff source terms. With our local space–time Galerkin predictor method, where nonlinear flux and source term are fully coupled in the predictor stage and where the *optimal* local space–time polynomial distribution is found due to the Galerkin orthogonality property, such problems have not been encountered. Therefore and for the sake of completeness, we show the convergence rates for the relaxed variable E_y in Table 2 for the schemes $P_0 P_2, P_0 P_3$ and $P_1 P_4$. We deduce from the results of Table 2 that the nominal order of accuracy is reached even for the electric field, which contains the stiff source term. This confirms the results already presented in [11], where uniform order of accuracy in space and time was found in the stiff as well as in the non-stiff case.

Concerning computational performance we must note that most of the CPU time is spent in the locally implicit predictor step, i.e. in the local space time discontinuous Galerkin scheme. The corrector step is not more expensive than any standard
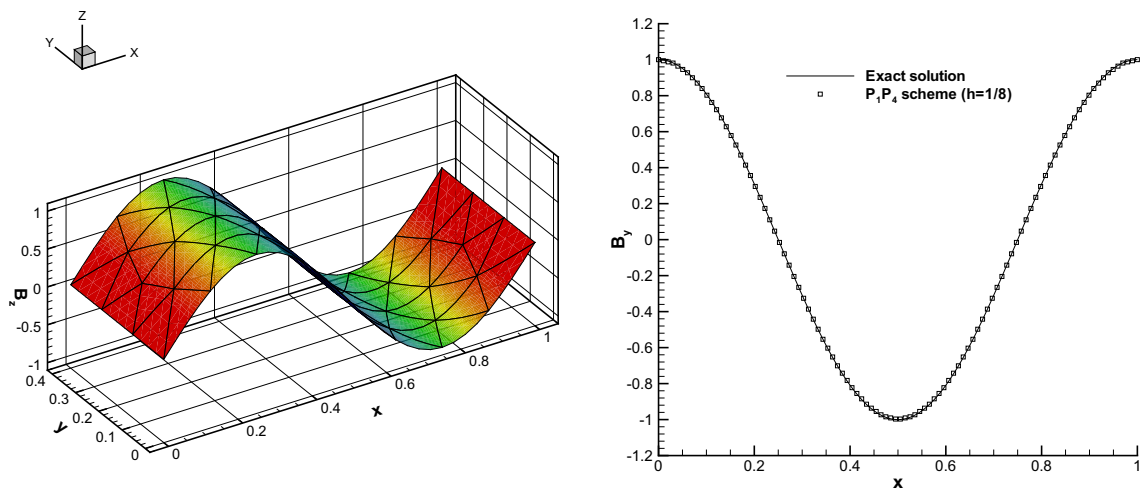

Fig. 1. Large amplitude Alfvén wave. Left panel: very coarse unstructured triangular mesh ($h = 1/8$) used for the fifth order $P_1 P_4$ scheme and surface plot of the quantity B_z at the final time $t = 2.618033988$. Right panel: comparison of exact and numerical solutions for B_y at the final time obtained with the $P_1 P_4$ scheme on the very coarse mesh. A cut along the line $y = 0$ is shown, evaluating the reconstructed polynomials on 100 equidistant points.

Table 1
Large amplitude Alfvén wave. Convergence study of $P_N P_M$ schemes from third to fifth order of accuracy. $\sigma = 10^7$, apart from the $P_1 P_4$ scheme where $\sigma = 10^8$. Errors are computed for variable B_y.

$P_0 P_2$			$P_1 P_2$			$P_2 P_2$		
N_G	L^2	$\mathcal{O}_{L^2}$	N_G	L^2	$\mathcal{O}_{L^2}$	N_G	L^2	$\mathcal{O}_{L^2}$
16	1.71E−02		8	9.12E−04		8	8.97E−04	
24	5.32E−03	2.9	12	2.26E−04	3.4	12	2.92E−04	2.8
32	2.26E−03	3.0	16	9.34E−05	3.1	16	1.67E−04	1.9
64	2.79E−04	3.0	24	2.53E−05	3.2	24	4.98E−05	3.0
$P_0 P_3$			$P_1 P_3$			$P_1 P_4$		
12	1.81E−03		4	7.18E−03		4	3.32E−03	
16	4.52E−04	4.8	8	3.75E−04	4.3	8	2.95E−05	6.8
24	7.35E−05	4.5	12	7.91E−05	3.8	12	4.46E−06	4.7
32	1.98E−05	4.6	16	2.82E−05	3.6	16	1.07E−06	5.0

Table 2
Large amplitude Alfvén wave. Verification of the order of accuracy for a variable affected by the stiff source term. We use the quantity E_y and some selected $P_N P_M$ schemes.

$P_0 P_2$			$P_0 P_3$			$P_1 P_4$		
N_G	L^2	$\mathcal{O}_{L^2}$	N_G	L^2	$\mathcal{O}_{L^2}$	N_G	L^2	$\mathcal{O}_{L^2}$
16	7.66E−03		12	6.09E−04		4	9.43E−04	
24	1.90E−03	3.4	16	2.11E−04	3.7	8	1.22E−05	6.3
32	7.75E−04	3.1	24	4.02E−05	4.1	12	2.06E−06	4.4
64	9.56E−05	3.0	32	1.14E−05	4.4	16	5.18E−07	4.8

explicit one-step finite volume or DG scheme. To give the reader the possibility to compare his own implementation with ours, we give the CPU times needed for all third order $P_N P_M$ schemes to update all variables of one element for one entire timestep using a value of $\sigma = 10^5$: The $P_0 P_2$ scheme with WENO needs 1.5 ms, the $P_1 P_2$ scheme needs 1.3 ms and the $P_2 P_2$ method also requires 1.3 ms. Computations were run on one core of an Intel Core 2 Dual CPU with 2.5 GHz clock speed and 4 GB of RAM.

4.2. Self-similar current sheet

This smooth test case was first proposed by Komissarov et al. [24], it has been presented also in Palenzuela et al. [29] and it provides a truely resistive test, far from the ideal MHD limit. It has the following exact analytical solution for the y-component of the magnetic field:

$$B_y(x, t) = B_0 \, \text{erf} \left(\frac{1}{2} \sqrt{\frac{\sigma}{t}} x \right), \tag{55}$$

where erf is the error function. The initial time for this test case is $t = 1$ and the initial condition at $t = 1$ is given by $\rho = 1$, $p = 50$, $\vec{E} = \vec{v} = 0$ and $\vec{B} = (0, B_y(x, 1), 0)^T$. We choose $\gamma = \frac{4}{3}$ and $B_0 = 1$. The conductivity is chosen as $\sigma = 100$, which means a moderate resistivity. The problem is solved with two different fourth order $P_N P_M$ schemes on the two-dimensional computational domain $\Omega = [-1.5; 1.5] \times [-0.5; 0.5]$, where we impose periodic boundary conditions in y-direction and Dirichlet boundary conditions consistent with the initial condition in x-direction. The first scheme is a pure finite volume method ($P_0 P_3$) using the component-wise WENO reconstruction proposed in [12], running on a mesh with $h = 3/32$, which corresponds to an equivalent one-dimensional resolution of 32 points. The second scheme is the $P_2 P_3$ method which is part of the new intermediate class of numerical schemes discovered in [10], running on a very coarse mesh with $h = 3/8$, i.e. using only eight points in the one-dimensional case. The mesh is depicted on the left panel of Fig. 2 together with a surface plot of the magnetic field in y-direction. Both numerical solutions are compared at time $t = 10$ with the exact solution given by Komissarov et al. [24] and Palenzuela et al. [29] on the right panel of Fig. 2. We note an excellent agreement with the exact solution and underline that the use of high order methods in *space and time* allows us to use very coarse meshes, compared to standard second order TVD schemes.

4.3. Shock tube problems

In this section we solve the fifth of a series of test problems proposed by Balsara in [1]. We solve the RRMHD equations with different values for the conductivity σ. The initial condition is given by two piecewise constant states separated by a discontinuity at $x = 0$. The left and right values for the primitive variables are reported in Table 3. Furthermore, we set
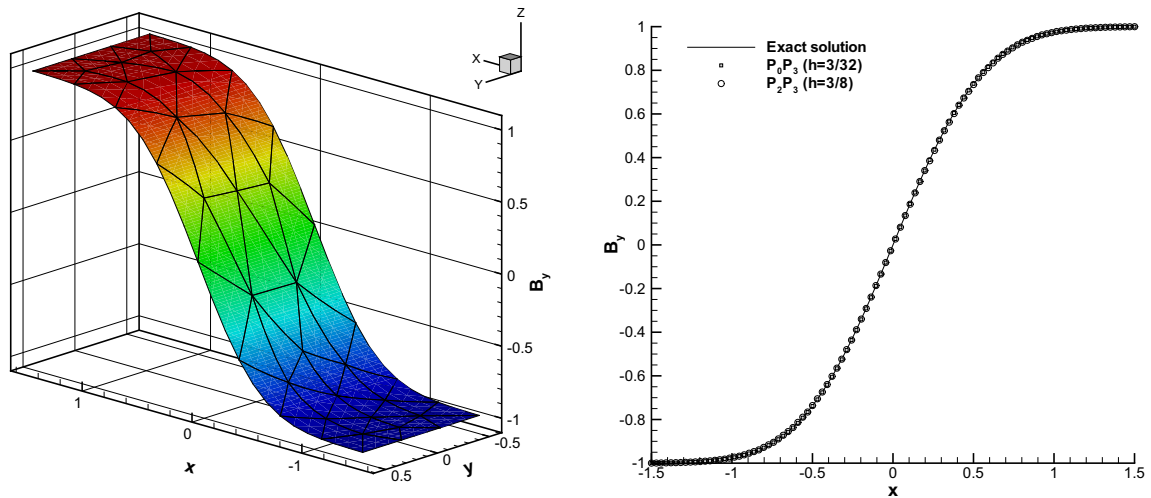
Fig. 2. Self-similar current sheet. Left panel: unstructured triangular mesh used for the P_2P_3 scheme and surface plot of the quantity B_y. Right panel: comparison of exact and numerical solutions at time $t = 10$ obtained with two different fourth order P_NP_M schemes on different meshes. A cut along the line $y = 0$ is shown, evaluating the reconstructed polynomials on 100 equidistant points.

Table 3
Initial states left (L) and right (R) for the relativistic MHD shock tube problem. The last column reports the final time t_e considered in the numerical test.

Case	ρ	p	u	v	w	B_y	B_z	B_x	t_e
L	1.08	0.95	0.4	0.3	0.2	0.3	0.3	2.0	0.55
R	1.0	1.0	−0.45	−0.2	0.2	−0.7	0.5	2.0	

$\vec{E} = -\vec{v} \times \vec{B}$, $\phi = \psi = q = 0$ and $\gamma = \frac{5}{3}$. The conductivities in our test cases are chosen as $\sigma = 0, \sigma = 1, \sigma = 10, \sigma = 10^2, \sigma = 10^3$ and $\sigma = 10^6$. The computational domain is $\Omega = [-0.5; 0.5] \times [0; 0.05]$ with periodic boundaries in y-direction and Dirichlet boundaries consistent with the initial condition in x-direction. We use an unstructured triangular mesh of characteristic size $h = 1/400$, which is depicted together with a surface plot of the density ρ in Fig. 3. A cut through the solution along the x-axis is shown in Fig. 4 for all different values of σ used in this series of test cases. The exact solution is the one for the ideal RMHD equations, as published in [15]. The essential wave structures of the ideal RMHD Riemann problem can be noted for $\sigma = 10^3$ or greater. For values below, the resistivity leads to a considerable diffusion of the discontinuities.

4.4. Rotor problem

In this section we solve a resistive relativistic version of the MHD rotor problem proposed by Balsara and Spicer [2]. Our computational setup is a variation of the ideal relativistic MHD rotor test case of Del Zanna et al. [36]. In contrast to [36], who solved the ideal RMHD equations on a perfectly regular Cartesian mesh, we solve this test case in Cartesian coordinates on a *circular* computational domain with radius $R = 0.5$ using an *unstructured triangular* mesh with a characteristic mesh spacing of $h = 0.004$ towards the center and $h = 0.005$ at the outer border of the domain, leading to a total number of 72,320 trian-
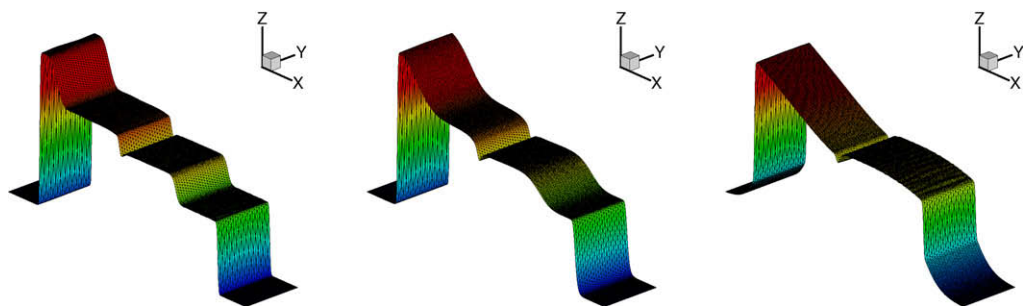

Fig. 3. RRMHD shock tube test problem using a P_0P_2 WENO scheme and different values for the conductivity σ. The unstructured triangular mesh is shown together with a surface plot of the density ρ. Left panel: $\sigma = 10^3$. Middle panel: $\sigma = 10^2$. Right panel: $\sigma = 10$. A cut along the line $y = 0$ is shown at 400 equidistant points.
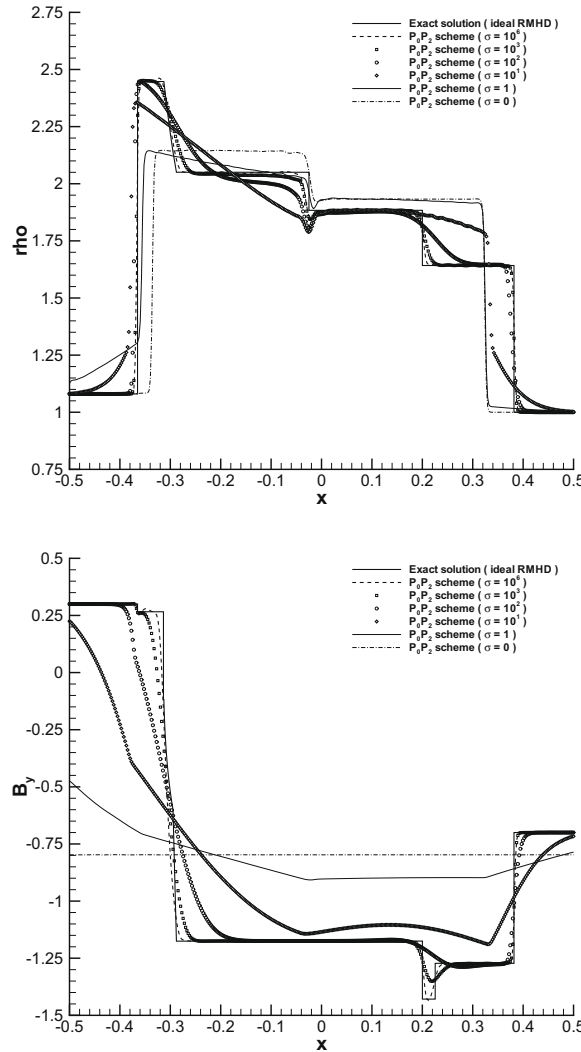
Fig. 4. RRMHD shock tube test problem using a P_0P_2 WENO scheme and different values for the conductivity σ. The exact solution is shown for the ideal RMHD equations. The density ρ is plotted on the top of the figure and the magnetic field component B_y on the bottom.

gles. The rotor has a radius of $R_0 = 0.1$ and is spinning with an angular frequency of $\omega_s = 8.5$, leading to a maximal toroidal velocity of $v_\phi = 0.85$. The density is $\rho = 10$ inside the rotor and $\rho = 1$ in the outer fluid at rest. The pressure is $p = 1$ and the magnetic field is $\vec{B} = (1, 0, 0)^T$ in the whole domain. The initial electric field is, as usual, computed as $\vec{E} = -\vec{v} \times \vec{B}$. We use a P_0P_2 scheme with component-wise WENO reconstruction. No taper is applied to the initial condition, as in [36], and $\gamma = 4/3$ is used. Transmissive boundary conditions are applied at the outer boundaries. The computational domain and the results for the pressure at time $t = 0.3$ are shown in Fig. 5 for different values of the electric conductivity. We solve the problem with $\sigma = 10$ and $\sigma = 10^5$ and, as a reference solution, we also show the results obtained with the ideal RMHD equations. The ideal RMHD results agree qualitatively very well with those obtained with the RRMHD equations using the larger conductivity $\sigma = 10^5$. For the case of a lower conductivity ($\sigma = 10$) one can clearly see that the wave structure is completely different, with a faster moving electric field that is governed directly by the Maxwell equations and no longer resulting from the relation $\vec{E} = -\vec{v} \times \vec{B}$ as in the ideal case.

4.5. Cylindrical explosion problem

We consider a cylindrical explosion problem, where the initial pressure exhibits a jump over three orders of magnitude. The domain Ω is again the circle of radius $R = 0.5$. The fluid is initially at rest ($\vec{v} = \vec{E} = 0$) and subject to a constant magnetic field $\vec{B} = (0.05, 0, 0)^T$. Within a circle of radius $r = 0.15$ the density and pressure are $\rho = p = 1$, whereas in the ambient fluid the density is $\rho = 0.1$ and the pressure is $p = 0.001$. We use a slightly more refined mesh than in the previous section, containing 76,514 triangles. We use again a P_0P_2 scheme with component-wise WENO reconstruction and $\gamma = 4/3$. The outer
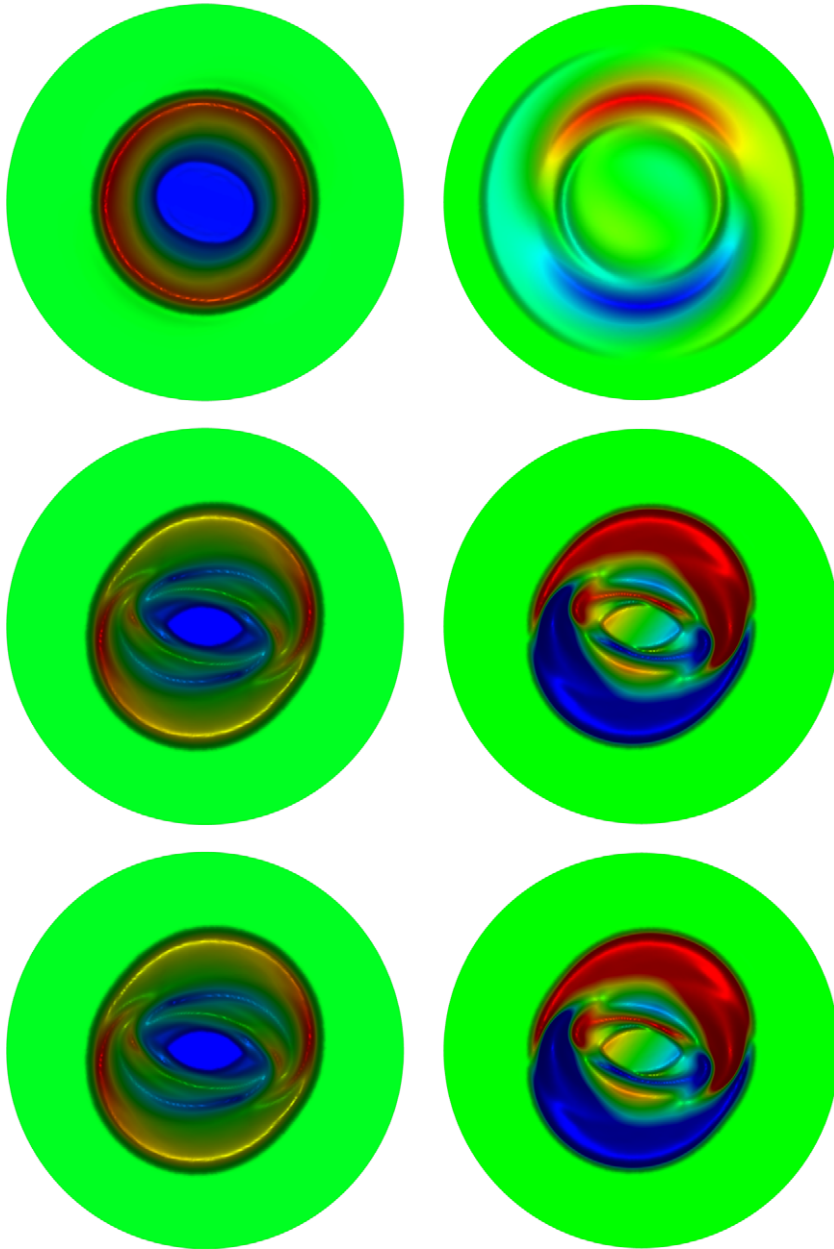
Fig. 5. Pressure field (left column) and electric field component E_z (right column) for the resistive relativistic rotor problem at time $t = 0.3$. Top: $\sigma = 10$. Middle: $\sigma = 10^5$. Bottom: ideal RMHD.

boundaries are transmissive. We have to underline that our initial conditions are milder than the ones of the test case proposed in [23]. This was necessary due to the fact that we are rigorously using a high order WENO scheme everywhere in the computational domain, without any switch that reduces the order of accuracy locally if strong shocks or other troubled cells occur. The original initial conditions proposed in [23] led in our scheme to unphysically high velocity values ($|\vec{v}| > 1$) in the subroutine that converts conservative to primitive variables. To make our scheme more robust in view of astrophysical applications we will investigate the use of a shock detector that locally reduces the method to a second order TVD scheme at strong shocks and in zones where velocities larger than the speed of light occur.

The computational results for our test problem are shown in Fig. 6 at time $t = 0.3$ for $\sigma = 10$ and $\sigma = 10^5$, as well as a reference computation obtained by solving the ideal RMHD equations. We find an excellent agreement between our resistive RMHD simulation with the large conductivity ($\sigma = 10^5$) and the ideal RMHD results. We note that for $\sigma = 10$ the amplitudes of the flow variables are lower than in the stiff case ($\sigma = 10^5$) and the ideal case due to the presence of physical resistivity.

4.6. Orszag–Tang vortex

The last of this series of test cases is a resistive relativistic analogous of the Orszag–Tang vortex problem [28] studied extensively in [6,30,19]. The computational domain is $\Omega = [0; 2\pi]^2$. The initial condition of the problem is given by

$$(\rho, u, v, p, B_x, B_y) = (1, -\sin(y), \sin(x), 1, -B_0 \sin(y), B_0 \sin(2x)), \tag{56}$$

with $w = B_z = 0$ and $\gamma = \frac{4}{3}$. The problem is solved up to $t = 4.5$ using a P_0P_2 scheme with component-wise WENO reconstruction on an unstructured triangular mesh with 55,292 elements ($h = \frac{1}{25}$). The results are shown for the pressure in Fig. 7 for times $t = 0.5, t = 2.0$ and $t = 4.5$ using two different values for the conductivity, $\sigma = 10$ and $\sigma = 10^3$. These rather low values for σ have been deliberately chosen in order to run our method also for at least one test case in a really resistive regime, far from the ideal RMHD assumptions.
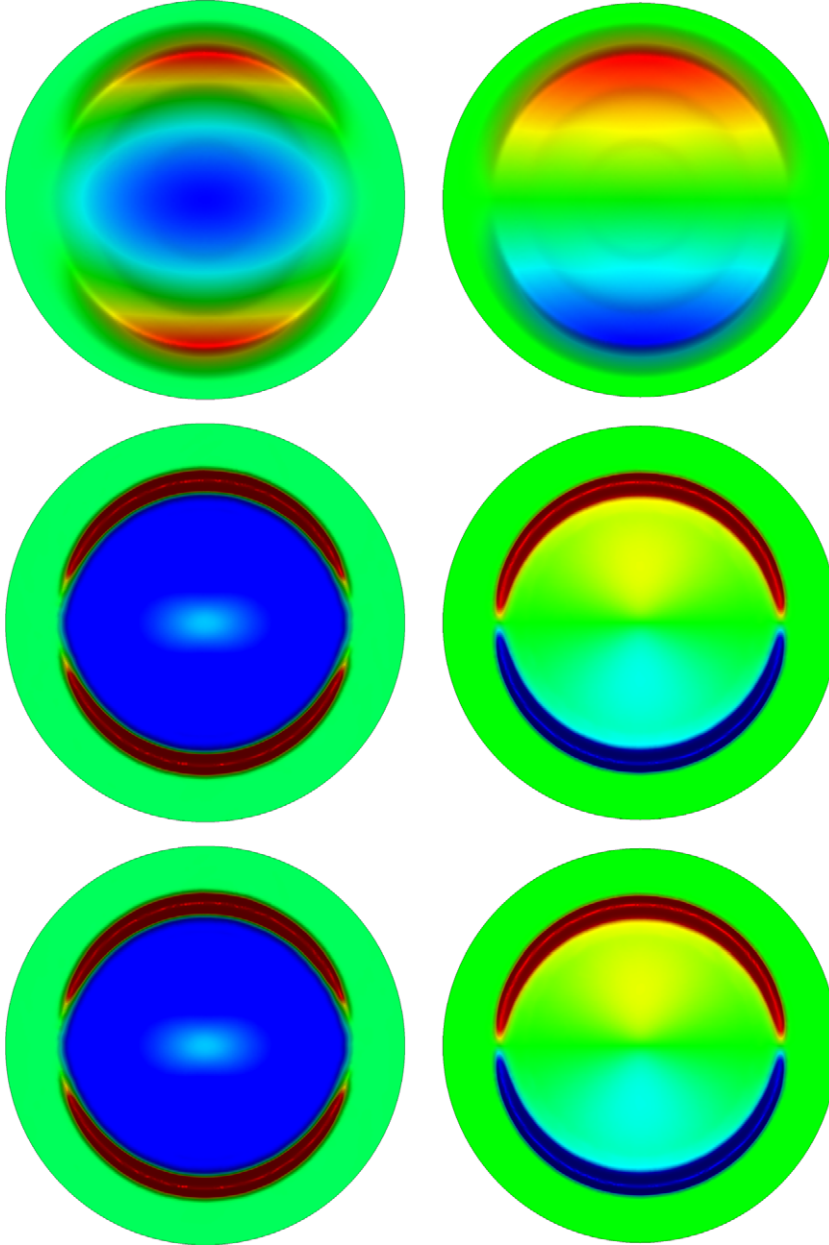

Fig. 6. Magnetic field component B_x (left column) and electric field component E_z (right column) for the resistive relativistic explosion problem at time $t = 0.3$. Top: $\sigma = 10$. Middle: $\sigma = 10^5$. Bottom: ideal RMHD.
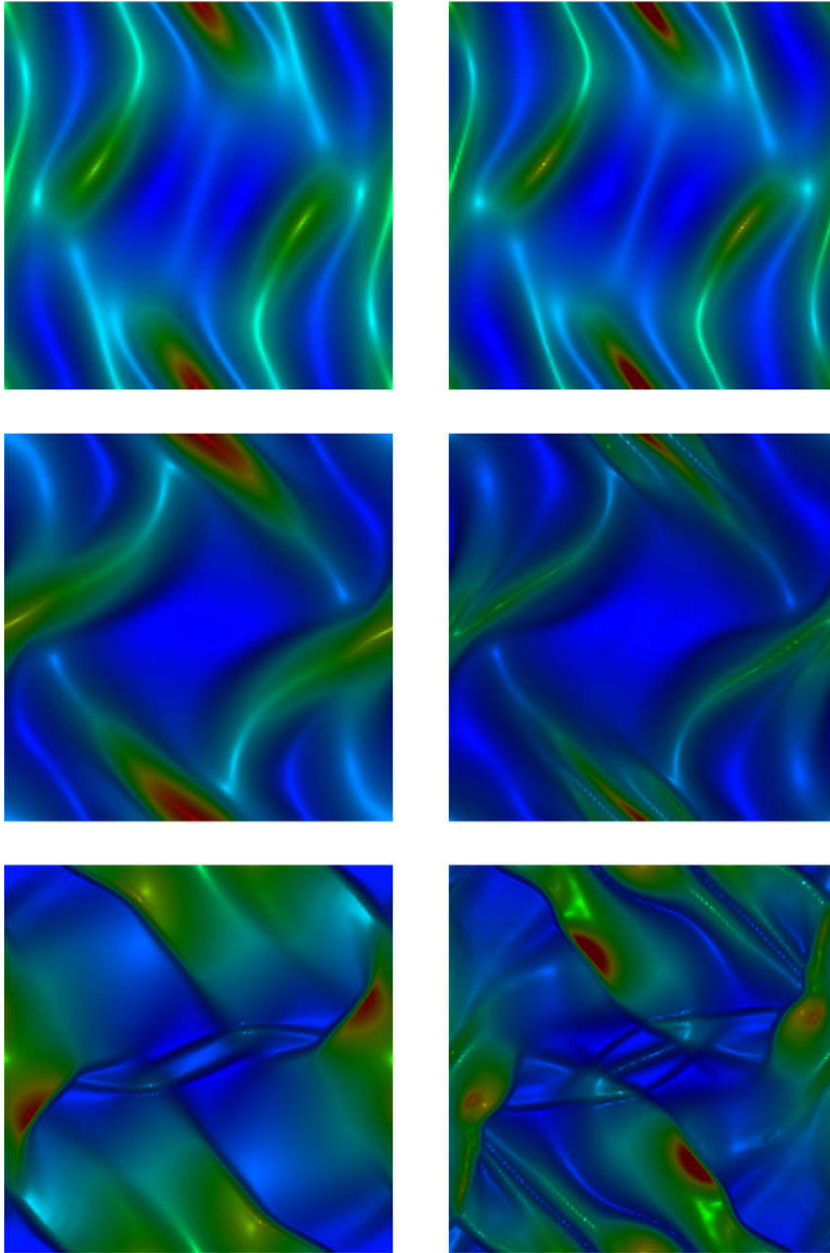
Fig. 7. Pressure field for the resistive relativistic Orszag–Tang vortex problem at times $t = 0.5$, $t = 2.0$ and $t = 4.5$ (from top to bottom). Left column: $\sigma = 10$. Right column: $\sigma = 10^3$.

As in the original problem [28], the smooth sinusoidal initial condition evolves in time to form complex shock dominated structures for the large value of the conductivity. For the lowest conductivity used here ($\sigma = 10$), one clearly notes the diffusion caused by the electric resistivity.

5. Conclusions

In this paper we have solved the resistive relativistic magnetohydrodynamics equations using the class of methods introduced in Dumbser et al. [10] and named $P_N P_M$ schemes. The equations present source terms that are potentially stiff when the ideal limit of infinite conductivity is recovered. As such, they are naturally accounted for through the application of the local space–time discontinuous Galerkin predictor, originally deviced in [11].

To our knowledge, the computations presented in this paper are the first better than second order accurate simulations *in space and time* ever done for the stiff limit of the RRMHD equations and the results obtained point to favor higher order methods over standard second order TVD schemes. In particular, the accuracy that can be achieved with high order $P_N P_M$ schemes on very coarse meshes makes them promising tools for simulations of physical processes that require high computational resources, such as a large class of time dependent problems involving magnetic reconnection in astrophysical context. Further directions of future improvement are represented by the generalization of the scheme into full general relativity as well as the inclusion of more complex Ohm's laws.

Acknowledgments

References

[1] D. Balsara, Total variation diminishing scheme for relativistic magneto-hydrodynamics, The Astrophysical Journal Supplement Series 132 (2001) 83–101.

[2] D. Balsara, D. Spicer, A staggered mesh algorithm using high order godunov fluxes to ensure solenoidal magnetic fields in magnetohydrodynamic simulations, Journal of Computational Physics 149 (1999) 270–292.

[3] D.S. Balsara, T. Rumpf, M. Dumbser, C.D. Munz, Efficient high accuracy ADER–WENO schemes for hydrodynamics and divergence-free magnetohydrodynamics, Journal of Computational Physics 228 (2009) 2480–2516.

[4] T.J. Barth, P.O. Frederickson, Higher order solution of the Euler equations on unstructured grids using quadratic reconstruction, in: AIAA Paper No. 90-0013, 28th Aerospace Sciences Meeting, January 1990.

[5] G. Cardano, Artis magnae sive de regulis algebraicis liber unus, Petreius, Nürnberg, Germany, 1545.

[6] R.B. Dahlburg, J.M. Picone, Evolution of the OrszagTang vortex system in a compressible medium. I. Initial average subsonic flow, Physics of Fluids B 1 (1989) 2153–2171.

[7] A. Dedner, F. Kemm, D. Kröner, C.-D. Munz, T. Schnitzer, M. Wesenberg, Hyperbolic divergence cleaning for the MHD equations, Journal of Computational Physics 175 (2002) 645–673.

[8] L. Del Zanna, O. Zanotti, N. Bucciantini, P. Londrillo, ECHO: a Eulerian conservative high-order scheme for general relativistic magnetohydrodynamics and magnetodynamics, Astronomy & Astrophysics 473 (October) (2007) 11–30.

[9] T. di Matteo, Magnetic reconnection: flares and coronal heating in active galactic nuclei, Monthly Notices of the Royal Astronomical Society 299 (August) (1998) L15+.

[10] M. Dumbser, D. Balsara, E.F. Toro, C.D. Munz, A unified framework for the construction of one-step finite-volume and discontinuous Galerkin schemes, Journal of Computational Physics 227 (2008) 8209–8253.

[11] M. Dumbser, C. Enaux, E.F. Toro, Finite volume schemes of very high order of accuracy for stiff hyperbolic balance laws, Journal of Computational Physics 227 (2008) 3971–4001.

[12] M. Dumbser, M. Käser, Arbitrary high order non-oscillatory finite volume schemes on unstructured meshes for linear hyperbolic systems, Journal of Computational Physics 221 (2007) 693–723.

[13] M. Dumbser, M. Käser, V. A Titarev, E.F. Toro, Quadrature-free non-oscillatory finite volume schemes on unstructured meshes for nonlinear hyperbolic systems, Journal of Computational Physics 226 (2007) 204–243.

[14] M. Dumbser, C.D. Munz, Building blocks for arbitrary high order discontinuous Galerkin schemes, Journal of Scientific Computing 27 (2006) 215–230.

[15] B. Giacomazzo, L. Rezzolla, The exact solution of the Riemann problem in relativistic magnetohydrodynamics, Journal of Fluid Mechanics 562 (2006) 223–259.

[16] A. Gruzinov, Power of an axisymmetric pulsar, Physical Review Letters 94 (2) (2005) 21101.

[17] A. Harten, B. Engquist, S. Osher, S. Chakravarthy, Uniformly high order essentially non-oscillatory schemes, III, Journal of Computational Physics 71 (1987) 231–303.

[18] C.H. Jaroschek, H. Lesch, R.A. Treumann, Relativistic kinetic reconnection as the possible source mechanism for high variability and flat spectra in extragalactic radio sources, Astrophysical Journal Letters 605 (April) (2004) L9–L12.

[19] G.S. Jiang, C.C. Wu, A high-order WENO finite difference scheme for the equations of ideal magnetohydrodynamics, Journal of Computational Physics 150 (1999) 561–594.

[20] A. Kandus, C.G. Tsagas, Generalized Ohm's law for relativistic plasmas, Monthly Notices of the Royal Astronomical Society 385 (April) (2008) 883–892.

[21] C. Klaij, J.J.W. Van der Vegt, H. Van der Ven, Space–time discontinuous Galerkin method for the compressible Navier–Stokes equations, Journal of Computational Physics 217 (2006) 589–611.

[22] S.S. Komissarov, On the properties of Alfvén waves in relativistic magnetohydrodynamics, Physics Letters A 232 (February) (1997) 435–442.

[23] S.S. Komissarov, Multidimensional numerical scheme for resistive relativistic magnetohydrodynamics, Monthly Notices of the Royal Astronomical Society 382 (December) (2007) 995–1004.

[24] S.S. Komissarov, M. Barkov, M. Lyutikov, Tearing instability in relativistic magnetically dominated plasmas, Monthly Notices of the Royal Astronomical Society 374 (2007) 415–426.

[25] Y.E. Lyubarsky, On the relativistic magnetic reconnection, Monthly Notices of the Royal Astronomical Society 358 (March) (2005) 113–119.

[26] M. Lyutikov, Magnetar giant flares and afterglows as relativistic magnetized explosions, Monthly Notices of the Royal Astronomical Society 367 (April) (2006) 1594–1602.

[27] M. Lyutikov, D. Uzdensky, Dynamics of relativistic reconnection, Astrophysical Journal 589 (June) (2003) 893–901.

[28] S.A. Orszag, C.M. Tang, Small-scale structure of two-dimensional magnetohydrodynamic turbulence, Journal of Fluid Mechanics 90 (1979) 129.

[29] C. Palenzuela, L. Lehner, O. Reula, L. Rezzolla, Beyond ideal MHD: towards a more realistic modeling of relativistic astrophysical plasmas, Monthly Notices of the Royal Astronomical Society (2009).

[30] J.M. Picone, R.B. Dahlburg, Evolution of the Orszag–Tang vortex system in a compressible medium. II. Supersonic flow, Physics of Fluids B 3 (1991) 29–44.

[31] R. Schopper, H. Lesch, G.T. Birk, Magnetic reconnection and particle acceleration in active galactic nuclei, Astronomy & Astrophysics 335 (July) (1998) 26–32.

[32] A.H. Stroud, Approximate Calculation of Multiple Integrals, Prentice-Hall Inc., Englewood Cliffs, NJ, 1971.
[33] V.A. Titarev, E.F. Toro, ADER schemes for three-dimensional nonlinear hyperbolic systems, Journal of Computational Physics 204 (2005) 715–736.
[34] D.A. Uzdensky, On the axisymmetric force-free pulsar magnetosphere, Astrophysical Journal 598 (November) (2003) 446–457.
[35] J.J.W. van der Vegt, H. van der Ven, Space–time discontinuous Galerkin finite element method with dynamic grid motion for inviscid compressible flows I. general formulation, Journal of Computation al Physics 182 (2002) 546–585.
[36] L. Del Zanna, N. Bucciantini, P. Londrillo, An efficient shock-capturing central-type scheme for multidimensional relativistic flows II. Magnetohydrodynamics, Astronomy and Astrophysics 400 (2003) 397–413.
[37] S. Zenitani, M. Hesse, A. Klimas. Two-Fluid MHD Simulations of Relativistic Magnetic Reconnection, ArXiv e-prints, February 2009.